



University
of Glasgow

Ivanisenko, Y. and MacLaren, I. and Sauvage, X. and Valiev, R.Z. and Fecht, H.-J. (2006) *Shear-induced $\alpha \rightarrow \gamma$ transformation in nanoscale Fe-C composite*. Acta Materialia, 54 (6). pp. 1659-1669. ISSN 1359-6454

<http://eprints.gla.ac.uk/4860/>

Deposited on: 15 January 2009

Shear-induced $\alpha \rightarrow \gamma$ transformation in nanoscale Fe-C composite.

Yu. Ivanisenko^{1*}, I. MacLaren², X. Sauvage³, R.Z. Valiev⁴

and H.-J. Fecht^{1,5}

¹ Institut für Nanotechnologie, Forschungszentrum Karlsruhe, 76021 Karlsruhe, Germany

² Department of Physics and Astronomy, University of Glasgow, Glasgow G12 8QQ, UK

³ Groupe de Physique des Matériaux UMR CNRS 6634, Institute of Material Research, University of Rouen BP 12, 76801 Saint-Etienne du Rouvray, France

⁴ Institute of Physics of Advanced Materials, Ufa State Aviation Technical University, 450000, Ufa, Russia

⁵ Division of Materials, Ulm University, 89081 Ulm, Germany

Abstract High-resolution transmission electron microscopy and 3D Atom Probe observations show clearly that reverse transformation of bcc ferrite to fcc austenite occurs during severe plastic deformation of a pearlitic steel resulting in a nanocrystalline structure; something which never occurs in conventional deformation of coarse-grained iron and steels. The driving force and the mechanisms of this reverse transformation are discussed. It shows that nanostructure and shear stresses are essential for this process, and confirms molecular dynamics (MD) predictions of such transformations in nanocrystalline iron.

1. Introduction

Processes of severe plastic deformation (SPD), i.e. high shear strains under high imposed pressure leading to strong grain refinement in metals and alloys realized in a number of mechanical methods including high pressure torsion of disc shaped samples, equal channel angular pressing, mechanical milling of powder samples, or the friction and wear induced

* Corresponding Author. Tel.: +49-72471-82-6961; fax: +49-7247-82-8298
E-mail address: ivanissenko@int.fzk.de (Yu. Ivanisenko)

transformation of the near-surface regions of heavily-worn materials such as high speed railway tracks and tool steels [1,2,3,4]. SPD processed bulk nanomaterials can demonstrate a remarkable combination of mechanical properties: very high strength and enhanced plasticity [5] and even low temperature superplasticity [6]. When applied to pearlitic steels, all these processing routes transform the initially lamellar structure to a homogenous nanocrystalline structure with a mean grain size as small as 10 nm accompanied by the total dissolution of cementite [4,7,8,9,10]. The resulting Fe-C nanocrystalline composite demonstrated values of hardness higher than that of conventional martensite [7,8], and its thermal stability is 200°C higher than that of martensite [11].

The phenomenon of strain-induced decomposition of iron carbide cementite, which is normally very stable at room temperature, draws attention to the problem of phase equilibrium in systems with small dimensions. Although this problem has already been studied for 100 years, it becomes particularly interesting now with increasing interest in nanocrystalline materials. Factors such as excess free energy due to the large volume fraction of interfaces in nanocrystalline materials compared with that in the bulk together with capillary effects may lead to changes in melting points [12,13], increases of solubility limits and displacement of the phase boundaries in phase diagrams [14,15]. In a somewhat different vein, Martin and co-workers [16,17] have shown that phase equilibrium can also be significantly shifted due to the application of external forces, that lead to formation of so called driven alloys with compositions far from those predicted from equilibrium phase diagrams. Martin *et al.* [16] argued that during plastic straining numerous ballistic jumps of atoms are occurring. These jumps are connected with dislocation glide, when all atoms above the gliding plane are shifted by one Burgers vector with respect to their neighbours below the plane after each dislocation pass. Therefore, contrary to the thermal jumps, these deformation induced jumps occur in a correlated manner and may result in second phase precipitation and dissolution, compound ordering and disordering, changes in crystallographic structure, and

even amorphisation [17]. It was shown recently that two factors: refinement of cementite lamellae down to the nanoscale [18,19] and strong deformation influence [8], lead to the destabilisation of cementite under plastic deformation resulting in its decomposition.

It now appears that the list of unusual phase transformations taking place in nanocrystalline pearlitic steel can be further extended. Recently we have presented an evidence of formation of austenite as a result of stress-induced reverse martensitic transformations due to severe plastic deformation of pearlitic steel [20]. In the present paper we discuss the thermodynamic driving force and atomistic mechanism of this shear phase transformation, as well as stability of the reverted austenite after release of stresses.

2. Material and experimental procedures

Nanocrystalline samples of pearlitic carbon steel UIC 860 (0.6-0.8 wt. % C, 0.8-1.3 wt. % Mn, 0.1-0.5 wt. % Si, 0.04 wt. % P (max), 0.04 wt. % S (max), Fe-balance) studied in the present investigation were obtained by High Pressure Torsion Deformation as described in [8]. In short, the sample was placed between two Bridgman anvils. The shear was realised by turning the lower anvil relative the fixed upper anvil at a speed $\omega = 1$ rpm. As with conventional torsion deformation, the shear strain γ can be estimated by means of the equation:

$$\gamma = \frac{2\pi NR}{h} \quad (1)$$

where: R is the distance from the sample centre, N is the number of the anvil rotations, and $h = 0.2$ mm is the thickness of the sample.

The samples investigated were rotated for $N = 5$ or 7 turns. Disk shaped specimens for thin foil preparation were cut out from the deformed disks in such a way that the transparent areas are situated at a distance of approximately 3 mm from the sample centre. At this distance from the centre, the shear strain γ is 300 for $N = 5$ turns.

Samples were prepared for transmission electron microscopy (TEM) by electropolishing with a 10% solution of HClO₄ at -15 °C at a voltage of 40V using a Tenupol 5 electropolishing apparatus (Struers A/S, Denmark). The resulting specimens were characterised by TEM using both conventional bright field imaging and high-resolution TEM (HRTEM) using a FEI Tecnai F20 operated at 200 kV, together with selected area diffraction (SAD) investigations in a FEI Tecnai T20 also operated at 200 kV, also equipped with a Gatan Image Filter (GIF). The crystallography of crystallites and the interfaces between them was determined from fast Fourier transforms (FFTs) of different areas of the HRTEM images.

3D atom probe (3D-AP) analysis was carried out at 80K under UHV conditions (residual pressure 10⁻⁸ Pa), with 20% pulse fraction and 1.7 kHz pulse repetition rate. The atom probe was equipped with a reflectron device to enhance the mass resolution and a CAMECA position sensitive detector (Optical Tomographic Atom Probe, OTAP). 3D-AP specimens were prepared by electropolishing (2% perchloric acid in 2-butoxyethanol, 15V, 293K). Small rods were cut in HPT discs and needle shaped specimens were prepared so that the tip was located at a distance of 2±0.5 mm from the disc center (see reference [21] for details).

X-ray diffractograms were obtained using Bragg–Brentano geometry in the synchrotron ANKA at Forschungszentrum Karlsruhe, and radiation with energy of 18.98 keV ($\lambda = 0.0653235$ nm) was chosen. The data were fitted by Pearson VII functions and the lattice parameter of ferrite was determined by means of the Nelson-Riley method [22].

3. Results

3.1 TEM and HRTEM observations

The microstructure of the steel after 5 rotations is homogenous and nanocrystalline, as shown in the bright-field TEM image of Fig. 1a. The SAD pattern from a small sample area (Fig. 1b) shows the strong Debye-Scherrer ferrite rings characteristic of polycrystalline

structures with very small crystallite sizes. This diffraction pattern is dominated by the strong diffraction rings from the ferrite (α) structure. Dark-field images of the ferrite could be produced using electrons from the 110 ring selected by a suitably small objective aperture and one such image is shown in Fig. 1c. This shows that the mean grain size of the ferrite is of the order of 10 nm, in accordance with our previous reports [8], and the morphology of the grains is primarily equiaxed with not a trace of lamellae in sight.

The SAD pattern of Fig. 1b was, however, recorded in the GIF and was energy-filtered using a 5eV slit around the zero-loss electrons thus excluding all electrons that have lost more than 2.5 eV from the image. Thus, the electrons that have lost energy through interactions with plasmons and which usually give a diffuse background in diffraction patterns have been excluded, meaning that weak spots are much more visible than normal. This, in addition to a little contrast enhancement and gamma correction makes clear that there are many more spots than just those due to the ferrite. Some of these are clearly due to residual cementite and have been labelled as such, and indexed where the indexing was unambiguous. A dark-field image of cementite was also obtained and shows occasional very fine equiaxed cementite particles distributed uniformly in the structure (Fig. 1d), with again no trace of the former lamellae. Our previous estimates of the cementite content in HPT pearlitic steel [7,8] had demonstrated that cementite had been completely dissolved; those estimates were made on the basis of the thermomagnetic measurements. Presumably, the discrepancy between the results of thermomagnetic analysis and the present TEM observations can be explained either by the tiny amount of the remaining cementite (<1%), which could be detected in the thermomagnetic measurements, or by the alteration of the magnetic properties of cementite as a result of deformation.

Surprisingly, there are also some reflections that could be interpreted as austenite (γ) reflections, as indicated and indexed on Fig. 1b, and several different diffraction rings could be identified. The largest d-spacing 111_γ ring could not be identified due to it having an

almost identical d-spacing to the 110_{α} ring. Attempts to isolate the austenite grains using the dark field technique failed because of the proximity of austenitic diffraction rings to the ferritic ones.

The imaging of some austenitic nanograins was, however, made possible by HRTEM, an example being shown in Figure 2a. The image displays two grains overlapping at a vertical interface. FFTs of the left and right hand regions are shown (Fig. 2, inserts: R corresponds to the right region and the L to the left one). The region on the left side shows two spots with 0.49 \AA^{-1} ($d = 2.027 \text{ \AA}$) and one with 0.6 \AA^{-1} ($d = 1.67 \text{ \AA}$). This pattern can be readily indexed as a $\langle 110 \rangle$ zone axis pattern for fcc-structured austenite. The right hand region shows spacing of 0.49 \AA^{-1} ($d = 2.027 \text{ \AA}$) for all spots and is thus a $\langle 111 \rangle$ ferrite region. The orientation relationship between the two phases is clearly the well-known Kurdjumov-Sachs orientation relationship [23]: $\langle 111 \rangle_{\text{bcc}} // \langle 110 \rangle_{\text{fcc}}$, $\{110\}_{\text{bcc}} // \{111\}_{\text{fcc}}$ (Fig. 2). The spacing of Moiré fringes at the interface between the two phases $9.5 \pm 0.05 \text{ nm}$ corresponds to the inverse of the spot splitting between, for example $(01\bar{1})_{\text{bcc}}$ and $(\bar{1}1\bar{1})_{\text{fcc}}$, which is $1.05 \pm 0.05 \text{ nm}^{-1}$ thus making it clear that such fringes arise at the overlap of suitably oriented ferrite and austenite grains. The interphase boundary plane probably represents the habit plane for the transformation from the ferrite to the austenite phase and is slightly inclined to the $(0\bar{1}1)_{\text{bcc}}$ plane (Fig. 2). The apparent width of the Moiré pattern is about 2 nm and the specimen is 10-20 nm thick, assuming a thickness of 15 nm, the misorientation from $(0\bar{1}1)$ would be 7.5° . It is worth emphasising that the habit plane for thermally induced $\alpha \rightarrow \gamma$ transformations in iron and in pearlitic steels of a similar composition to the steel studied in present work is also slightly inclined to the $(0\bar{1}1)_{\text{bcc}}$ plane [24,25].

A further unusual observation is shown in Figure 3, which is an HRTEM image of the boundary between two ferritic grains (bcc_1 and bcc_2) with an orientation relationship of $\langle 001 \rangle_{\text{bcc}_1} // \langle 111 \rangle_{\text{bcc}_2}$, $(1\bar{1}0)_{\text{bcc}_1} // (1\bar{1}0)_{\text{bcc}_2}$. Both grains are rotated about 54.7° around a

$\langle 110 \rangle$ axis. This does not correspond to any simple twin relationship or coincidence site lattice (CSL) relationship and possible reasons for appearance of such an unusual orientation will be discussed later.

3.2 *Lattice parameter of ferrite.*

The precise determination of the ferrite lattice parameter using synchrotron radiation revealed a slight, but significant increase of the lattice parameter $a_{\alpha\text{-Fe}}$: after HPT, $a_{\alpha\text{-Fe}} = 2.86682 \pm 0.00005 \text{ \AA}$, as compared to $a_{\alpha\text{-Fe}} = 2.8664 \text{ \AA}$ prior HPT. This corresponds to approximately 0.1 at.% or 0.025 wt.% of carbon in solid solution after HPT[26].

3.3 *3D-AP investigation.*

3D-AP data of a pearlitic steel with a similar composition prior to deformation have already been reported in previously published papers [19,21]. In the $\alpha\text{-Fe}$ phase the measured carbon concentration was below 0.1 at. %, while in the cementite lamellae (Fe_3C carbides) it was always very close to 25 at. %.

After severe plastic deformation by HPT up to 5 turns, the original structure has dramatically changed and new features appear. In some regions, nanoscale carbon rich lamellae are exhibited (figure 4a). Their thickness is in the range of 5 to 10 nm and the interlamellar spacing in a range of 10 to 20 nm. The carbon concentration profile computed across these lamellae clearly shows that they contain only about 4 at. % carbon (figure 4b). Such a low amount indicates that they might be former Fe_3C lamellae, which have been dissolved during the deformation. Unfortunately, the crystallography of this nanoscale structure cannot be determined from 3D-AP data. However, it is interesting to note that the fcc austenite observed by HRTEM could contain such a high amount of carbon in solid solution. The large carbon gradients exhibited by the composition profile could also indicate that carbon atoms may have diffused significant distances in the ferrite phase during deformation.

As a result of the Fe₃C dissolution, large volumes with a high concentration of carbon in solid solution were also analysed (figure 4c). The carbon concentration is in a range of 0.5 to 2 at.%, and gradients seem to indicate that long range bulk diffusion of carbon occurred during the deformation (figure 4d). Such zones could be austenite grains as observed by HRTEM.

4. Discussion

4.1 Evidence of reverse martensitic transformation

The observation of even small quantities of austenite in heavily deformed pearlitic steel, which by definition contained no austenite prior to the deformation, indicates that some form of reverse transformation of ferrite to austenite has occurred. The two phases are related by the well-known Kurdjumov-Sachs orientation relationship, which is often associated with martensitic transformations. Therefore there can be only two mechanisms explaining such transformation: one is that the temperature rose higher than the eutectoid temperature T_0 , which is 580°C at a deformation pressure of 7 GPa [27], either due to the adiabatic heating of the whole specimen [28] or due to formation of the adiabatic shear bands [29], followed by subsequent quenching. The observed austenite would be therefore the austenite retained after the martensitic transformation on cooling. The only other possibility is that a reverse martensitic transformation has occurred.

The present experiment was performed at room temperature and due to the good thermal contact between the thin specimen and massive anvils there is a rapid outflow of any heat arising from the deformation. We can thus discount any significant bulk heating of the sample arising from the deformation. There, however, remains the possibility that significant local heating could occur in adiabatic shear bands, and a recent study has estimated extremely high temperature rises of over 1000°C in adiabatic shear bands in a pearlitic steel, albeit at rather higher strain rates, namely four orders of magnitude larger, than used in the present

study [30]. It is well known that plastic deformation of pearlitic steels usually accompanies localisation of deformation. This occurs because cementite lamellae are obstacles for the propagation of dislocations in ferrite, and deformation localises first in colonies favourably oriented with respect to the direction of the shear stresses [31]. In the course of straining, randomly oriented colonies rotate to align along this direction. Such behaviour is common to wire drawing [18,31], cold rolling [32], and high-pressure torsion [8]. Generally it is known that shear localization is associated with a local softening of the structure. This softening can be due to *thermal*, but also due to *geometrical* reasons. In geometrical softening, the structure orients itself to a direction that is easier (i.e., requires less stress) for glide [33]. Exactly such re-orientation is observed in case of plastic deformation of pearlitic steels with conventional strain rates [8,18,31,32]. In contrast to geometrical softening, in thermal softening the local increase in temperature can result in a softening that leads to localization. In the extreme case when the *strain rate is so high* ($>10^3 \text{ s}^{-1}$) that the local heat generated cannot escape from the deformation area the adiabatic shear bands are formed. The equivalent strain rate in present experiments is much lower and corresponds to $\sim 0.5 \text{ s}^{-1}$ for the areas located at the 3 mm distance from the specimen centre¹. It is thus clear that a thermal origin of the austenite can be excluded. In the absence of other realistic possibilities, we conclude that the austenite in this severely plastically deformed steel must have been formed via a reverse martensitic transformation.

Nevertheless, two areas must be considered in relation to this, namely the crystallographic and atomistic mechanisms that would effect such a transformation and the thermodynamics that would drive it.

4.2. *Driving force of the reverse transformation*

¹ Equivalent strain rate is estimated using von Mises criterion for shear strain γ : equivalent strain $e = \gamma/\sqrt{3}$.

The driving force for any martensitic transformation consists of two terms: the chemical driving force, representing the requirement for the difference in the free Gibbs energies of transforming (parent) phase and new phase to be equal to zero: $F^P(T_0) - F^N(T_0) = \Delta F(T_0) = 0$, and non-chemical one, necessary for nucleation and growth of new phase in the matrix. It has been shown that different factors may affect the phase equilibrium between parent and new phase: chemical composition and hydrostatic stress [34], and also introduction of a large amount of defects in the microstructure of parent phase that increase its free energy [35,36,37]. The non-chemical driving force can be provided either by a certain degree of undercooling/overheating or by external shear stress [34,38].

In the particular case of HPT deformation of nanocrystalline ferrite the following factors influence the phase equilibrium by decreasing the difference in the Gibbs free energy between ferrite and austenite: the nanocrystalline character of the microstructure of the steel and the high applied pressure. As it has been shown through a variety of methods [35-37], a crystal can be destabilized and removed from equilibrium under conditions of external forcing to form non-equilibrium phases, such as for example, extended solid solutions and highly-defective nanocrystalline, amorphous or glass-like structures. In the present case, the free energy of nanocrystalline oversaturated ferrite after HPT deformation is much higher than that in coarse grained state: the enthalpy release during heating of the HPT processed steel was 44.2 J/g or 2.5 kJ/mol (Fig. 5), which corresponds to more than 60% of the free energy difference between austenite and ferrite under normal conditions (4 kJ/mol, see Fig. 9 in Appendix I). Of course, a small part of this enthalpy was stored in austenitic grains and was used for their re-transformation to ferrite upon heating. However, the amount of these austenitic grains was about 1-2 %, thus this contribution is rather negligible. The value of 2.5 kJ/mol also corresponds to typical energies stored in nanostructured materials due to grain boundary effects [39]. So we conclude that the disorder localized within the large number of grain boundaries has a major impact towards the increase of the overall energy. This increases

the energetic ground level of the ferrite considerably and thus reduces the bcc-fcc transformation temperature, T_0 , accordingly.

The applied pressure of 7 GPa decreases the thermodynamic equilibrium temperature T_0 to 580°C in this steel [27] in addition to the changes caused by the nanostructured state discussed above. It is possible to estimate the corresponding decrease in ΔF caused by applied pressure [38]:

$$\Delta F_P = \varepsilon \cdot \sigma \quad (2)$$

where σ is a hydrostatic stress, and ε is the normal (volume) strain component of the invariant-plane shape (martensitic) transformation. In iron and steels of composition close to the studied in present work, $\varepsilon = -0.03$ (minus means that $\alpha \rightarrow \gamma$ transformation accompanies decrease in volume) [40] and σ is numerically negative when the normal stress is compressive. Then it is easy to estimate that $\Delta F_{P=7\text{GPa}} = 1.5$ kJ/mol. Obviously, summation of the contributions from the nanocrystalline structure and the applied pressure roughly results in decreasing of the difference of the free Gibbs free energy between austenite and ferrite by 4 kJ/mol, which exactly corresponds to the difference in free energies under normal conditions at room temperature and pressure. Therefore the room temperature difference in free energy between nanocrystalline ferrite and austenite under applied pressure of 7 GPa is close to zero, which makes the $\alpha \rightarrow \gamma$ transformation thermodynamically possible.

But martensitic transformations require additional energy to occur for the nucleation and propagation of the new phase in the matrix. This further driving force for the reverse martensitic transformation is provided by shear stresses at HPT. According to Patel and Cohen [38], this contribution is:

$$\Delta F_S = \tau \cdot \gamma \quad (3)$$

where τ is the shear component of the applied stress, resolved along a habit plane and γ is the shear component of the martensitic strain. In iron and steels of composition close to the

studied in present work, $\gamma = 0.236$ along the habit plane. τ is always taken to be positive because the many permutations virtually permit shearing in either sense, thus shear stresses will **always** stimulate the transformation. In our HPT experiments, the maximal shear stresses act in the plane normal to the axis of rotation, i.e. in the foil plane (Fig. 6), and we observe the reverse martensitic transformation mainly in bcc crystallites having the [111] zone axis parallel to the foil normal. The apparent habit plane in Figure 2a is almost perpendicular to this and makes a small angle with $(0\bar{1}1)_{\text{bcc}}$. According to the von Mises criterion, the yield stress in torsion τ_y is less than that in uniaxial tension σ_y as:

$$\tau_y = \frac{1}{\sqrt{3}} \sigma_y \quad (4)$$

and the σ_y of the nanocrystalline steel can be approximately estimated using the well-known relationship between Vickers hardness and yield stress [41]:

$$\sigma_y \approx HV/3 \quad (5)$$

where HV is the Vickers hardness. The hardness of the HPT processed steel is HV ~10 GPa [8], and τ_y is thus at least 2 GPa, but it could be even higher due to strain concentration in areas next to the boundary between ferrite and the remnants of cementite platelets. Thus the contribution of shear stresses to the driving force of transformation is ≥ 3.37 kJ/mol (Eq. 3) in favourably oriented grains, which is much larger than typical value of driving force for martensitic transformation in steels of 1.2 kJ/mol [40]. An estimate of the decrease of the austenite start temperature (A_s) due to applied shear stress at HPT shows that such high stresses alone can decrease the A_s by ~500K (see Appendix I) !

The above estimates show, that applied pressure and external shear stress contribute significantly to the change of energy balance between ferrite and austenite under HPT conditions. Nevertheless, after unloading ferrite becomes the more energetically stable room temperature phase again. The consequences thereof shall be discussed in 4.4.

It may also be noted that continued deformation of the steel after the formation of austenite in a region may increase the shear stress to a level that favours deformation by a shear transformation back to the ferrite phase. Nevertheless, as long as the austenite content is small, this is likely to be a minority process in comparison to the formation of austenite from ferrite by the above-discussed stress-induced martensitic transformation.

4.3 Mechanism of transformation

Previous studies have shown that reverse martensitic transformations can occur in steels and other ferrous alloys under certain conditions. The crystallographic and atomistic details of the transformations almost certainly differ from one study to another, depending on alloy composition and experimental conditions in much the same way as significant differences in the habit plane and orientation relationship may be found for the direct gamma-alpha martensitic transformations in different steels and ferrous alloys. Of all the studies, the closest composition to that studied in the present work is the pearlitic steel studied by Schastlivtsev *et al.* [25]. It may, therefore, be the case that a similar shear occurred in the present work to that deduced by Schastlivtsev *et al.* on the $(110)_{\text{bcc}}// (111)_{\text{fcc}}$ plane. Similarly, earlier work on rapid heating of iron whiskers also showed that the complementary shear plane for the reverse $\text{bcc} \rightarrow \text{fcc}$ transformation was $(110)_{\text{bcc}}$ although the shear direction was unknown [24]. Such a shear on a (110) plane is schematically illustrated in Figure 7 and it is shown that a shear of $1/6 [1\bar{1}0]_{\text{bcc}}$ on each plane would transform the bcc ABAB stacking sequence to a fcc-like ABCABC stacking sequence. The resulting structure would still be slightly distorted from cubic but could then be transformed to fcc-cubic by the application of an appropriate atomic relaxation. Depending on the exact form of the relaxation, a Kurdjumov-Sachs orientation relationship or a Nishiyama-Wassermann orientation relationship could result.

The precise atomistic mechanism for the nucleation and growth of the austenite martensite is unclear. Different models have been advanced for this in conventional martensites. Some account for martensite growth as essentially a shear or twinning based process [40] where others see the process in terms of discrete transformation dislocations / ledges [42]. It can be shown that glide of $1/6 \langle 1\bar{1}0 \rangle_{\text{bcc}}$ partials on every (110) plane will convert bcc stacking sequence to a fcc-like stacking sequence (Fig. 7). The separation distance for partials has been shown to increase under high stress [43]. It is just possible that such unusual $1/6 \langle 1\bar{1}0 \rangle_{\text{bcc}}$ partials may be emitted from interfaces under conditions of high stress where the thermodynamics already favours a martensitic reverse transformation to austenite. Nucleation may occur at defects, at interfaces, at dislocation pileups, or possibly from partial dislocations. The evidence suggests that different mechanisms may well be applicable in different alloys. In the present case, the paucity of dislocations in the grains would make a nucleation mechanism based on dislocation interactions unlikely. It may well be that the preferred sites for the nucleation of reverse martensitic transformation are grain boundaries and the regions close to the ferrite-cementite interphase boundaries. Due to the difference in deformability of ferrite and cementite [44], strong incompatibility stresses will develop at these boundaries [45] making the reverse transformation even more likely.

Recent studies using molecular dynamic techniques with an embedded atom method potential have shown a similar atomistic mechanism operating in conditions of high shear stress in nanocrystalline iron. This forced phase transformation results in a metastable displacive shear transition of bcc iron to closely packed fcc and hcp phases [46,47]. The orientation relationships between the transformed and untransformed regions were found to be similar to those observed for temperature-driven martensitic transformations in Fe and steels, and exactly the same as observed in the present study.

4.4 *Stability of austenite nanograins*

Some words should be said about the stability of the reverted austenite after unloading. The free energy of austenite is higher than that of nanocrystalline ferrite (section 4.2), thus austenite should be transformed back to ferrite immediately after unloading. The fact that we do observe some reverted austenite indicates that several stabilizing factors are operating in this particular case of pearlitic steel. According to our previous results [7,8], as well as to present data obtained thanks to 3D AP, severe plastic deformation leads to dissolution of carbides in pearlitic steels. Since the solubility of carbon in austenite is more than 20 times higher than that in the ferrite, carbon atoms would be readily diffuse in fcc areas if their mobility is high enough. Such an increase of the carbon content would help to stabilize the austenite with regard to ferrite. Actually, the observed in present experiment carbon supersaturated volumes with carbon concentration of about 0.5-2 at.% (Fig. 4c), which is much higher than room temperature solubility limit of carbon in ferrite, are likely the austenite grains. This conclusion is consistent with the precise determination of the ferrite lattice parameter using the synchrotron radiation. A slight increase of the ferrite lattice parameter, detected after HPT deformation, corresponds to the dissolution of approximately 0.15 at.% of carbon in ferrite lattice. Therefore it is reasonable to conclude that observed 0.5-2 at. % areas correspond rather to austenite than to ferrite. Other factors may also contribute to the stabilization of austenite, including the constraint and strain from surrounding crystals, the small size of the crystals resulting in little energetic advantage in transforming the crystal to conventional α' martensite, and the lack of suitable nuclei for this martensitic transformation.

However, we have found some evidence that such reversion does happen. The formation of the unusual orientation relationship between two ferritic grains in Fig. 4 may be explained by such double bcc \rightarrow fcc \rightarrow bcc transformation. If one supposes that after unloading the austenite has transformed back to ferrite having a different orientation to the original

orientation chosen from the 24 variants allowed by Kurdjumov-Sachs orientation relationship or the 12 variants allowed by Nishiyama-Wasserman orientation relationship. This can result in the rotation of the new bcc grain by 54.7° about $\langle 110 \rangle$ with respect to the original grain. A perfect example of this is shown in the simulations of Latapie and Farkas [46] where they show that in pure iron after reverse bcc \rightarrow fcc transformation, the fcc regions are then transformed back to the bcc having another crystallographic orientation. The schematic diagram of such transformation sequence is shown in Figure 8: the original ferritic grain (bcc₁) transforms to the transitional austenitic phase (fcc), and then this austenitic phase transforms to the new ferritic grain (bcc₂). The original ferritic grain and transitional austenitic phase are in the Nishiyama–Wasserman orientation relationship, and transitional austenitic phase and new ferritic grain are in the Kurdjumov-Sachs orientation relationship. One can see that orientation relationship between the grains in Fig. 3b completely identical to the OR between the grains bcc₁ and bcc₂ in the MD simulations of reference [46], and thus we provide the first direct experimental evidence for the existence of the processes shown in the simulation study.

4.5 *Reverse martensitic transformation as a new deformation mechanism in NC materials*

Stress induced martensitic transformation is well known in material science and is usually regarded as an additional deformation mechanism, which can substantially enhance the ductility of alloys [38,34]. Such a feature of martensitic transformation is utilized in case of TRIP (transformation induced plasticity) steels and shape memory alloys.

It was predicted theoretically and confirmed in experiments that the deformation mechanisms operating in NC materials are often radically different from those in coarse-grained materials, see for example a comprehensive review [48]. This leads, in general, to an increase of the mechanical strength by a factor 4 to 5 and a slight decrease in the Young's modulus [5,49,50]. A variety of mechanisms have been proposed to explain this behaviour,

including the difficulty of generating and propagating dislocations through the nanoscale grains and the large volume fraction of grain boundaries. Therefore, alternative deformation modes must be relevant for nanocrystalline materials, such as grain boundary sliding, grain rotation, grain boundary triple junction activities, stacking fault formation and deformation twinning.

In this respect the reverse martensitic transformation reported in the present work represents a new deformation mechanism, which can operate only in nanocrystalline iron and iron-based alloys and other material with polymorphic transformations.

5. Conclusions

For the first time, a stress-induced $\alpha \rightarrow \gamma$ transformation in nanocrystalline ferrite as a consequence of severe plastic deformation at the room temperature was experimentally demonstrated. Nanocrystalline grains of austenite 10-20 nm in diameter are formed having a Kurdjumov-Sachs orientation relationship with the neighboring ferrite. This was concluded to have occurred due to a stress-induced reverse martensitic transformation, and this additionally confirms earlier predictions of such transformations in MD simulations.

The increase of the Gibbs free energy of ferrite due to formation of the nanocrystalline structure and the dissolution of carbides together with high shear stresses under HPT provide the driving force for this reverse martensitic transformation. The atomistic mechanism of such transformation is likely to proceed by glide of ordered arrays of transformation partials $1/6\langle 1\bar{1}0 \rangle_{\text{bcc}}$ in every (110) plane.

Stress-induced austenite is an unstable phase at room temperature, and it will usually transform back to ferrite on unloading, often with another crystallographic orientation to the orientation of original ferrite. Therefore this stress induced phase transformation provides a new mechanism for grain rotation in nanostructured iron and iron-based alloys as a result of plastic deformation. However, there may be several factors allowing the retention of some

portion of the reverted austenite including dissolved carbon, residual strain and constraints from neighboring crystals, small crystallite size, and lack of suitable nuclei for this transformation.

The stress induced $\alpha \rightarrow \gamma$ phase transformation represents a new deformation mode that can be activated when alternative deformation mechanisms such as slip of lattice dislocations have become blocked by the nanostructure.

Acknowledgements: The authors are grateful to H. Rösner for very valuable comments on the manuscript and kind assistance in performing TEM and HRTEM experiments. We acknowledge financial support by the Landesstiftung Baden-Württemberg within the Network of Competence „Functional Nanostructures“ and Project B6 and the European Bulk Metallic Glass Project (BMG HPRN-CT-2000-00033).

Appendix I. Estimation of the decrease of the austenite start temperature (A_s) due to applied shear stress at HPT.

It is well known that external stress can induce both direct and reverse martensitic transformations by increasing the temperature of direct transformation (M_s) and decreasing the temperature of reverse one (A_s), respectively [34,38]. Hornbogen [34] has shown that an external shear stress τ with a component parallel to the transformation shear strain γ will raise or lower the transformation temperature, depending on its sign as:

$$\frac{d\bar{\tau}}{d\Delta T} = \frac{s_{\alpha\gamma}}{\gamma} \quad (6)$$

where $s_{\alpha\gamma}$ is the entropy of transformation. The entropy of transformation, $d\Delta F^{\gamma \rightarrow \alpha}/dT$, $\Delta F^{\gamma \rightarrow \alpha}$ is a difference in the free energy of the two phases, and can be approximately determined

from the temperature dependence of the free energy difference in the $\alpha \rightarrow \gamma$ transformation of the Fe-0.8 wt. % steel. The chemical free energy changes accompanying the $\alpha \rightarrow \gamma$ transformation were calculated for pure iron by Kaufmann and Cohen [51], and for the Fe-C interstitial solid solution by Imai *et al.* [52]. Fig. 9 represents the plot of the $\Delta F^{\gamma \rightarrow \alpha}(T)$ dependence for the Fe-0.8 wt.% steel. Using the curve in Fig. 9:

$$S_{\alpha\gamma} = \frac{d(F^\gamma - F^\alpha)}{dT} = 6.7 \text{ J/mol}\cdot\text{K}$$

This slope holds for the linear portion of the curve and prevails for the temperature range of interest (300 K). It should be stressed that this estimation of transformation entropy is very rough because the influence of the applied pressure was not included. It is assumed here that applied pressure decreases the transformation temperature, and, consequently the transformation energy, but does not change the slope of the $\Delta F^{\gamma \rightarrow \alpha}(T)$ curve significantly.

Thus the decrease in A_S due to an applied shear stress of $\tau_y = 2 \text{ GPa}$ can straightforwardly be estimated as:

$$\Delta A_S = \frac{\overline{\tau}_y \cdot \overline{\gamma}}{S_{\gamma\alpha}} = 503 \text{ K} \quad (7)$$

in favourably oriented ferritic grains.

References:

- [1] Valiev RZ, Islamgaliev RK and Alexandrov IV. *Progr in Mat Sci* 2000;45:103.
- [2] Zehetbauer M, Valiev RZ, eds. *Nanomaterials by Severe Plastic Deformation: Fundamentals–Processing–Applications - NanoSPD2, Proceedings of NANOSPD Conference*. Weinheim: J.Wiley VCH, 2002.
- [3] Fecht H-J, In: Edestein AS and Cammarata RC, editors. *Nanomaterials: Synthesis, Properties, and Application*. Bristol: Institute of Physics, J.W. Arrowsmith LTD, 1996.
- [4] Lojkowski W, Djahanbakhsh M, Bürkle G, Gierlotka S, Zielinski W and Fecht H-J, *Mater Sci Eng* 2001;A303:197.
- [5] Valiev RZ, *Nature mater.* 2004;3:511.
- [6] McFadden SX, Mishra RS, Valiev RZ, Zhilyaev AP, Mukherjee AK. *Nature* 1999;398:684.
- [7] Korznikov AV, Ivanisenko YuV, Laptionok DV, Safarov IM, Pilyugin VP, Valiev RZ. *NanoStructured Materials* 1994;4:159.
- [8] Ivanisenko Yu, Lojkowski W, Valiev RZ, Fecht H-J. *Acta Mater.* 2003;51:5555
- [9] Xu Y, Umemoto M, Tsuchiya K. *Materials Transactions* 2002;9:2205.
- [10] Ohsaki S, Hono K, Hidaka H, Takaki S, *Scripta Mater* 2005;52:271.
- [11] Ivanisenko Yu, Wunderlich R, Valiev RZ, Fecht H-J, *Scripta Mater.* 2003;49:947.
- [12] Dahmen U, Xiao SQ, Paciornik S, Johnson E, Johansen A. *Phys. Rev. Lett.* 1997;78:471.
- [13] Rösner H, Scheer P, Weissmüller J, Wilde G. *Philos. Mag. Lett.* 2003;83:511.
- [14] Yavari AR, Desre PJ, and Benameur T, *Phys Rev Lett* 1992;68:2235.
- [15] Weissmüller J, Bunzel P, Wilde G. *Scripta Mater* 2004;51:813.
- [16] Martin G, Bellon P. *Solid State Physics* 1996;50:189.
- [17] Chaffron L, Le Bouar Y, Saint-Ayes G, Martin G. *La Revue de Métallurgie* 2003;100 :183.

- [18] Languilaumme J, Kapelski G, and Baudelet B. *Acta Mater* 1997;45:1201.
- [19] Sauvage X, Copreaux J, Danoix F, and Blavette D. *Phil Mag* 2000;4:781.
- [20] Ivanisenko Yu, MacLaren I, Valiev RZ, Fecht H-J. *Adv. Eng. Mat.* 2005;10.
- [21] Sauvage X, Dacosta G, Valiev RZ, *Ultrafine Grained Materials III*, TMS (The Minerals, Metals & Materials Society), 2004 ;31.
- [22] Klug HP, Alexander LE. *X-ray diffraction procedures – 2 ed.* New York: Wiley, 1974.
- [23] Kurdjumov G, Sachs G. *Z Phys* 1930;64:325.
- [24] Zerwekh RP, Wayman CM. *Acta Metal.* 1965;13:99
- [25] Schastlivtsev VM, Yakovleva IL, Tabatchikova TI and Mirzaev DA, *J Phys. IV* 1995;5:531.
- [26] Burns JL. *Trans. AIME* 1934;113:239.
- [27] Hillard JE. *Trans. AIME* 1963;227:429.
- [28] Agarwala RP, Wilman H. *Proc Phys Soc.* 1953;66B:717.
- [29] Barry J, Byrne G. *Mat Sci Eng A* 2002;A325:356.
- [30] Syn CK, Lesuer DR and Sherby OD: *Materials Science and Technology* 2005;21:317.
- [31] Langford G. *Metallurgical Transactions A* 1977;8A:861
- [32] Gridnev VN and Gavriilyuk VG. *Phys Metals* 1982;4:531.
- [33] Meyers MA. *Plasticity: Adiabatic Shear Localization*. In: Buschow KHJ, Cahn RW, Flemings MC, Ilshner B (print), Kramer EJ, Mahajan S (Eds.), *Encyclopedia of Materials: Science and Technology*. 2001 Elsevier, pp. 7093-7103.
- [34] Hornbogen E. *Acta Metall.* 1985;33:595.
- [35] Fecht H-J, Johnson WL. *Nature* 1988;334:50.
- [36] Fecht H-J. *Nature* 1992;356:133.
- [37] Fecht H-J. *Phys Rev Lett.* 1990;65:610.
- [38] Patel JR. Cohen M. *Acta Metal.* 1953;1:531.

- [39] Fecht H-J. Nanostructured materials and composites prepared by solid state processing. In: Koch CC. (Ed.) Nanostructured Materials: Processing, Properties and Potential Applications, 2002 Noyes Publications, pp. 73-107
- [40] Nishiyama Z. Martensitic transformations. New York: Academic Press, 1978.
- [41] Ashby MF, Jones DRH. Engineering materials 1: an introduction to their properties and applications. 2nd ed. Oxford: Butterworth-Heinemann, 1996.
- [42] Olson GB, Cohen M, in: Dislocations in Solids. ed. Nabarro FRN. Amsterdam: North-Holland Physics Publishing, 1986, pp. 295-408.
- [43] Hirth JP, Lothe J. Theory of dislocations. New York: Wiley, 1982.
- [44] Langford G. Metallurgical Transactions A 1977;8A:861.
- [45] Ivanisenko YuV, Lojkowski W, Valiev RZ, Fecht H-J. Solid State Phenomena 2003;94:45.
- [46] Latapie A, Farkas D. Modelling Simul. Mat Sci Eng A 2003;11:745.
- [47] Kadau K, German TC, Lohmdahl PS, Hollian BL. Science 2002;296:1681.
- [48] Wolf D, Yamakov V, Phillpot SR, Mukherjee AK, Gleiter H. Acta Mater. 2005;53:1.
- [49] Weertman JR, Farkas D, Hemker K, Kung H, Mayo M, Mitra R, Van Swygenhoven H. MRS Bull 1999;24:44.
- [50] Koch C.C., ed. Nanostructured Materials: Processing Properties, and Potential Applications (Noyes Publications, NY 2002).
- [51] Kaufman L, Cohen M. Trans AIME 1956;206:1393.
- [52] Imai Y, Izumiyama M, Tsuchiya M. Sci Rep RITU 1965;17:173.

Figure captions

Figure 1. TEM micrographs of the microstructure of the steel after HPT deformation: (a) bright field image; (b) zero-loss filtered SAD pattern, ferrite rings are labelled and indexed, some cementite reflections are indicated, and austenite reflections are indexed; (c) dark field image using the 110 reflection of ferrite; (d) dark field image created using the some of the cementite reflections.

Figure 2. (a) HRTEM image of two overlapping grains. The beam direction is parallel to $[111]_{\text{BCC}}$ and $[110]_{\text{FCC}}$; b) FFT of the overlap region with the spot patterns from both crystals indicated showing the orientation relationship of the two crystals; c) indexed FFT of the region to the left of the boundary indicated with a dotted box; d) indexed FFT of the region to the right of the boundary indicated with a solid box.

Figure 3. (a) HRTEM image and (b) a diagram showing corresponding atomic structure of two neighbouring ferritic grains in HPT-processed steel. Inserts in (a) show corresponding FFTs. The orientation relationship between these grains is $\langle 001 \rangle_{\text{bcc1}} // \langle 111 \rangle_{\text{bcc2}}$, $(1\bar{1}0)_{\text{bcc1}} // (1\bar{1}0)_{\text{bcc2}}$. This corresponds to a misorientation at the boundary of $[1\bar{1}0]$, 54.7° .

Figure 4-a

3D reconstruction of an analysed volume ($10 \times 10 \times 37 \text{ nm}^3$) in the pearlite processed by HPT (5 turns). Only carbon atoms are plotted to show three carbon rich lamellae.

Figure 4-b

Carbon concentration profile computed from the left to the right across carbon rich lamellae exhibited in the figure 4-a. The carbon concentration of these lamellae is only about 4at.%.

Figure 4-c

3D reconstruction of an analysed volume ($11 \times 11 \times 34 \text{ nm}^3$) in the pearlite processed by HPT (5 turns). Only carbon atoms are plotted.

Figure 4-d

Carbon concentration profile computed across the 3D volume in the figure 4-c along the arrowhead direction. The exhibited carbon gradient seems to indicate that carbon long range diffusion occurred during the plastic deformation.

Figure 5. DSC curves of UIC 860 steel after HPT deformation. The integrated total enthalpy release is 44.2 J/g for the temperature range of 100-500°C.

Reprinted from [11] with permission of Elsevier.

Figure 6. Schematic diagram of the HPT specimen indicating how the thin foil was cut out. The Direction of applied pressure (P), maximal shear stresses (τ_{\max}) and incident electron beam for TEM investigations are indicated.

Figure 7. Schematic diagram of the bcc-fcc shear transformation. Arrows show the shear of the (110) plane of the bcc lattice by $1/6[1\bar{1}0]$ transforming the stacking into (111) fcc. Atomic layer A lies in the paper plane and layers B and C (C for fcc lattice) lie one and two layers out of the plane of the paper, respectively.

Figure 8. Schematic diagram of the sequence of stress-induced phase transformations in NC iron: original ferritic grain (bcc_1) transforms to transitional austenitic phase (fcc), and then this austenitic phase transforms to new ferritic grain (bcc_2). The original ferritic grain and transitional austenitic phase are in the Nishiyama–Wasserman orientation relationship ($\langle 110 \rangle_{\text{bcc}_1} // \langle 110 \rangle_{\text{fcc}}$ and $\{110\}_{\text{bcc}_1} // \{111\}_{\text{fcc}}$), and the transitional austenitic phase and the new ferritic grain are being in Kurdjumov-Sachs orientation relationship ($\langle 111 \rangle_{\text{bcc}_2} // \langle 110 \rangle_{\text{fcc}}$, $\{110\}_{\text{bcc}_2} // \{111\}_{\text{fcc}}$). After [26].

Figure 9. A graph of the change in free energy as a result of the γ - α transformation of Fe-0.8 wt.% C (3.43 at.% C) steel.

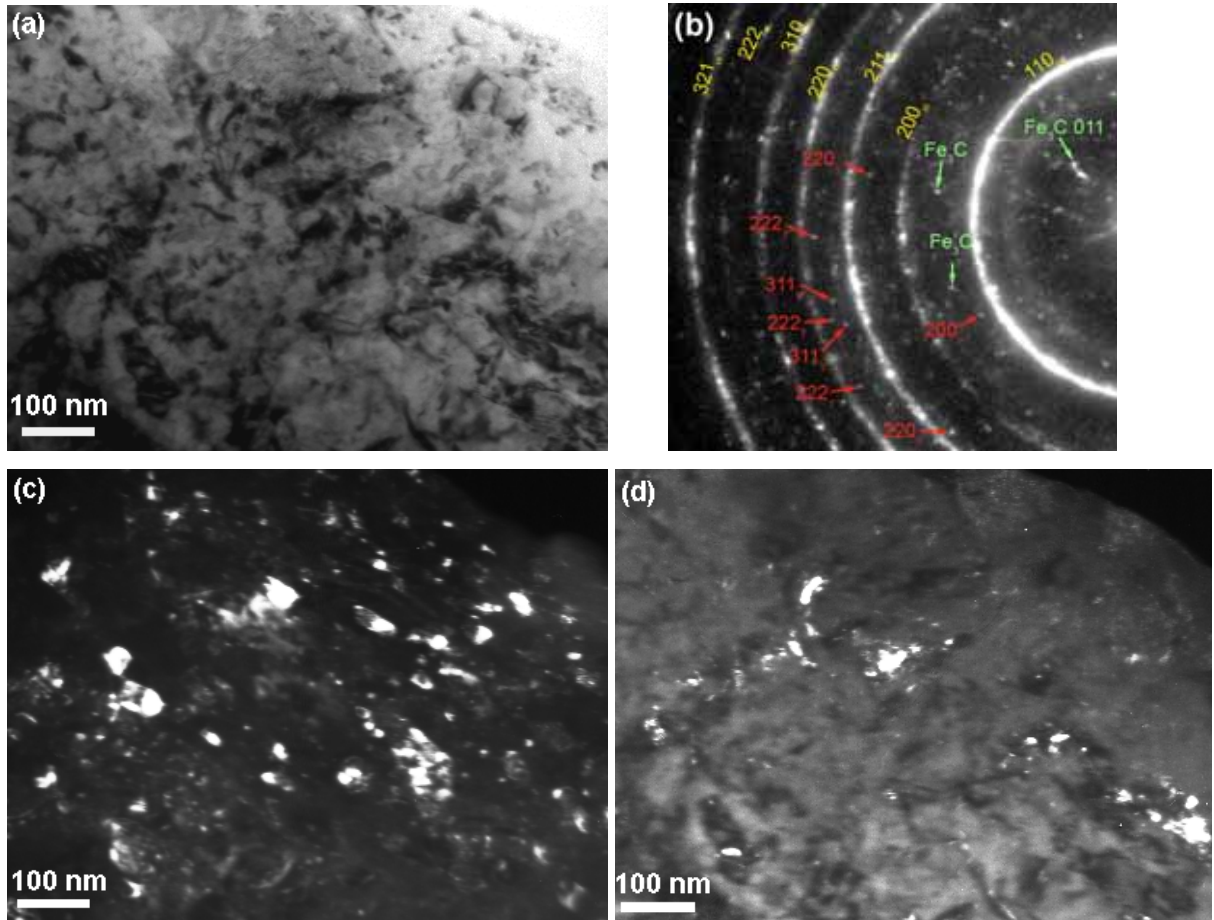


Figure 1.

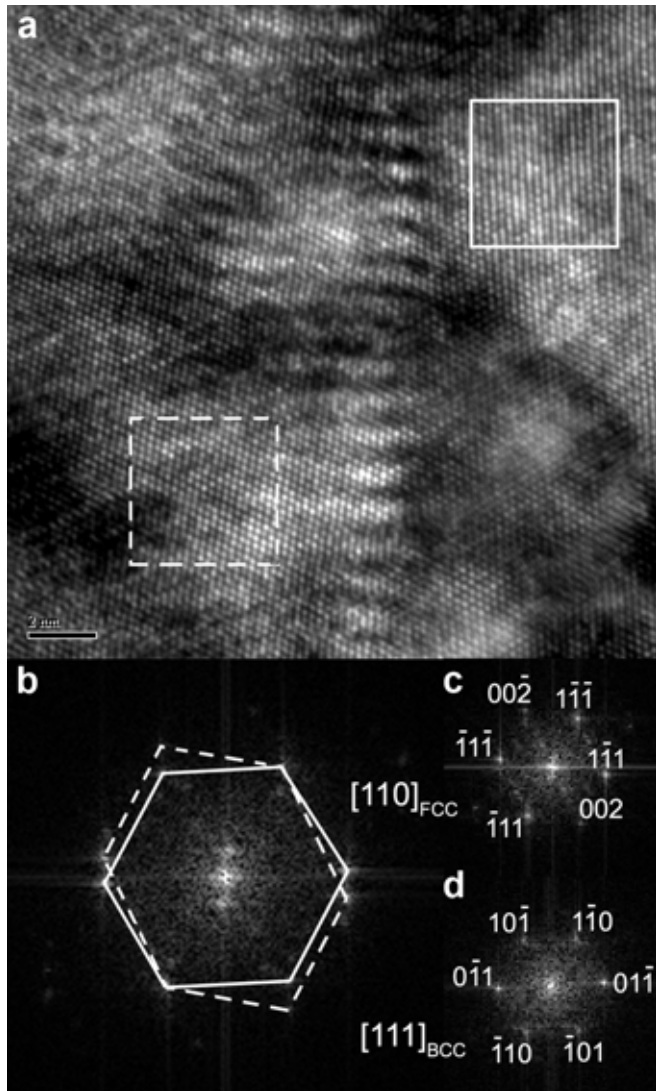


Figure 2.

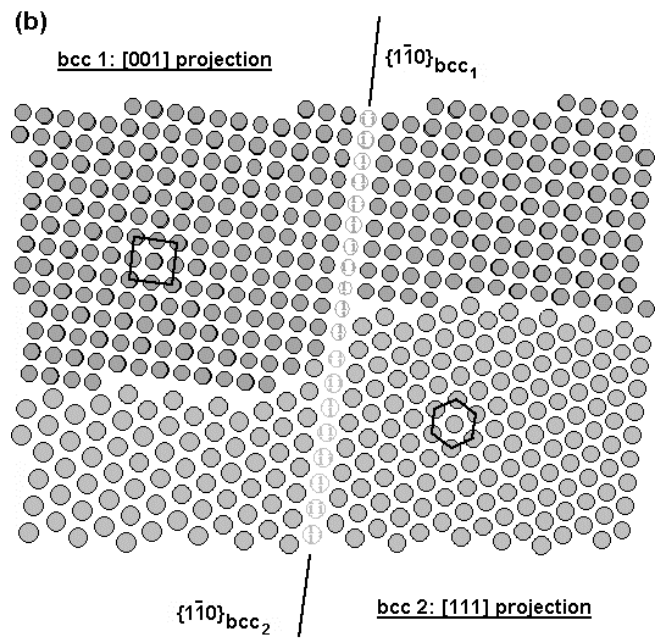
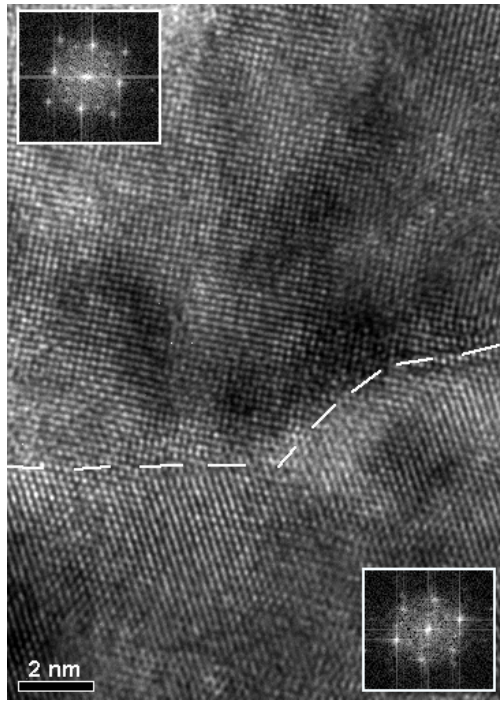


Figure 3.

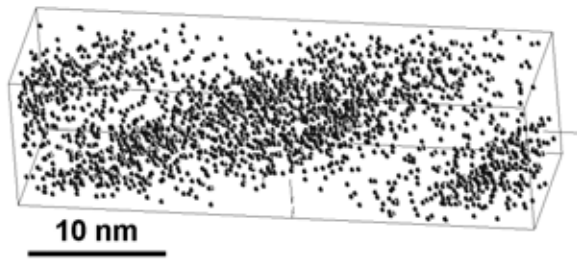


Figure 4a

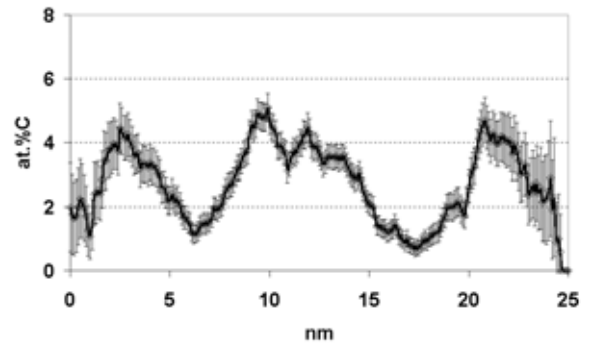


Figure 4b

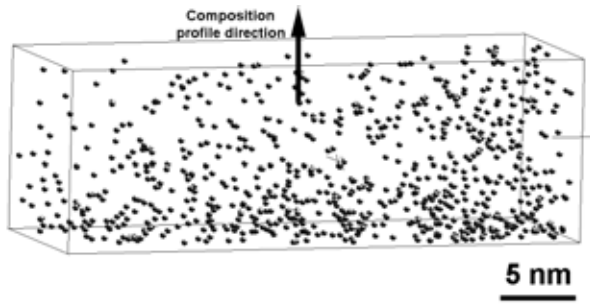


Figure 4c

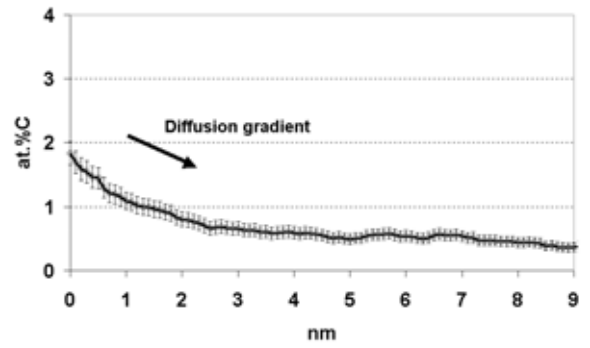


Figure 4d

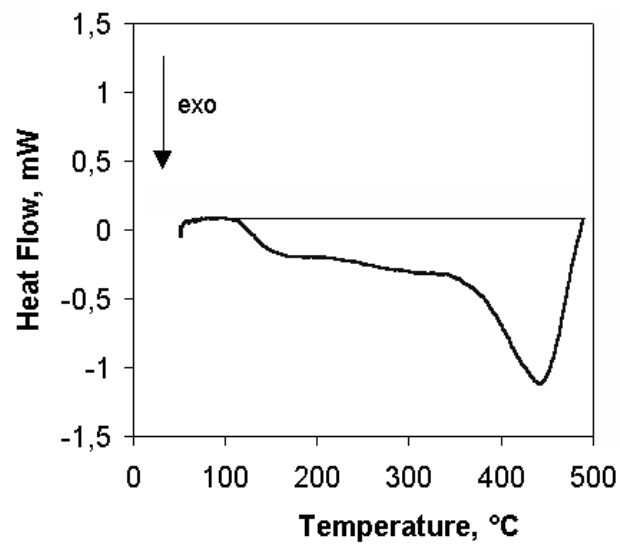


Figure 5.

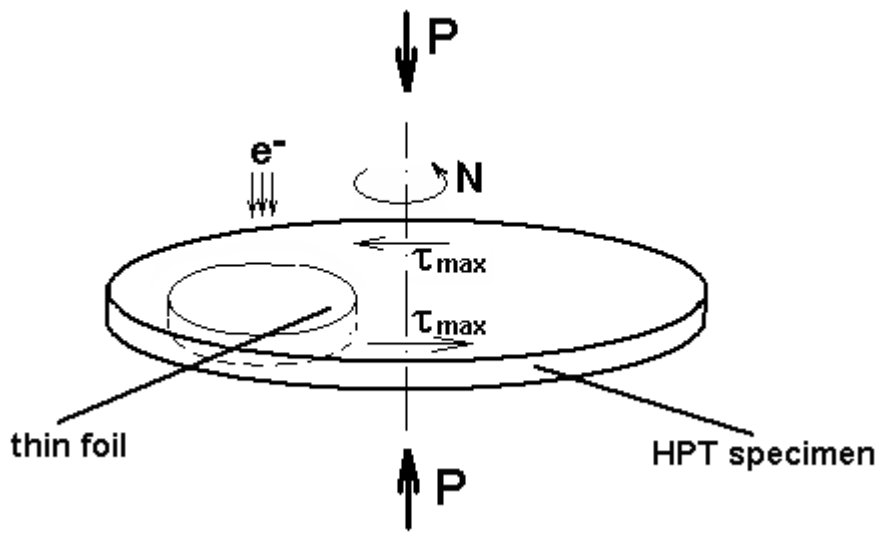


Figure 6.

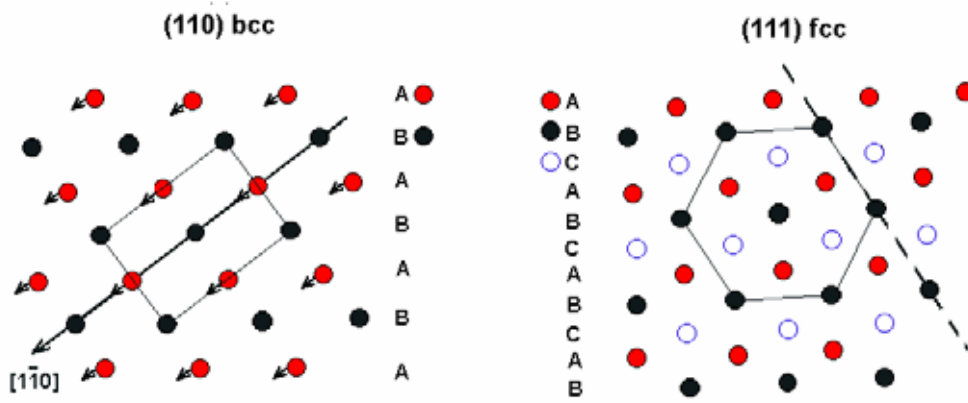


Figure 7.

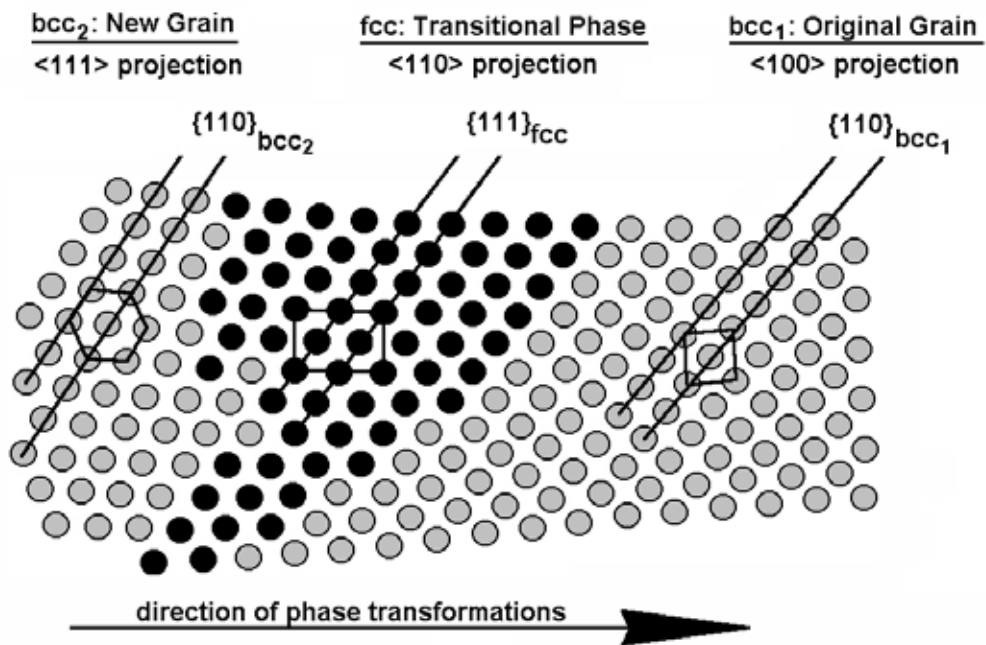


Figure 8.

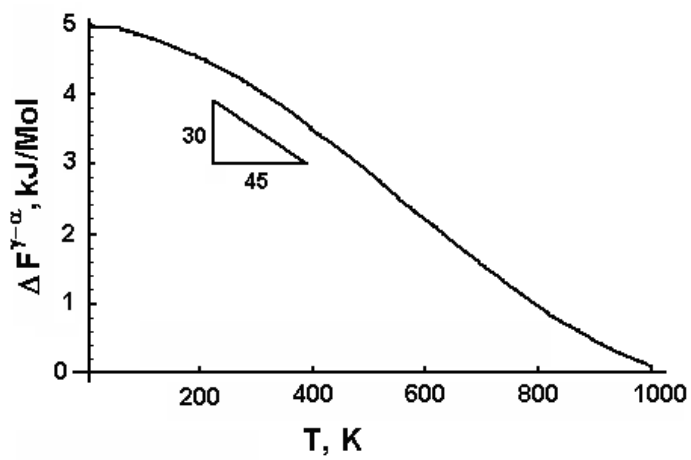


Figure 9.